

## Supplementary Information for

# **Cu-doping SnO<sub>2</sub>-NiO p-n Heterostructure for Significant Raman Enhancement with EF > 10<sup>10</sup>: Toward Ultrasensitive VOCs Sensing**

**Yan Zhou<sup>1</sup>, Qingyi Gu<sup>2</sup>, Tianzhu Qiu<sup>3</sup>, Xiao He<sup>2,5</sup>, Jinquan Chen<sup>1</sup>, Ruijuan Qi<sup>4</sup>, Rong Huang<sup>4</sup>, Tingting Zheng<sup>2\*</sup> and Yang Tian<sup>1,2\*</sup>.**

<sup>1</sup>State Key Laboratory of Precision Spectroscopy, East China Normal University, Dongchuan Road 500, Shanghai 200241, China.

<sup>2</sup>Shanghai Key Laboratory of Green Chemistry and Chemical Processes, Department of Chemistry, School of Chemistry and Molecular Engineering, East China Normal University, Dongchuan Road 500, Shanghai 200241, China.

<sup>3</sup>Oncology department, Jiangsu Province Hospital, Guangzhou Road 300, Nanjing 210000, China.

<sup>4</sup>Key laboratory of Polar Materials and Devices (MOE), Department of Optoelectronics, East China Normal University, Dongchuan Road 500, Shanghai 200241, China.

<sup>5</sup>Shanghai Engineering Research Center of Molecular Therapeutics and New Drug Development, School of Chemistry and Molecular Engineering, East China Normal University, Shanghai, 200062, China.

\*Correspondence sent to [tzheng@chem.ecnu.edu.cn](mailto:tzheng@chem.ecnu.edu.cn); [ytian@chem.ecnu.edu.cn](mailto:ytian@chem.ecnu.edu.cn).

**This PDF file includes:**

## **1 Supplementary Methods**

## **2 Supplementary Figures**

**2.1 Size distribution of SnO<sub>2</sub>-NiOx/Cu.**

**2.2 Characterization of SnO<sub>2</sub> and SnO<sub>2</sub>-NiO.**

**2.3 Raman spectra for calculation of EFs on SnO<sub>2</sub>, SnO<sub>2</sub>-NiO and SnO<sub>2</sub>-NiOx/Cu.**

**2.4 Mott-Schottky plots and SAED patterns of SnO<sub>2</sub>-NiOx/Cu.**

**2.5 XPS survey spectrum of SnO<sub>2</sub>-NiOx/Cu.**

**2.6 TDR spectroscopic measurements.**

**2.7 Determination of band gaps.**

**2.8 Effect of p-n heterojunction on Raman enhancement.**

**2.9 EM effect on SERS enhancement.**

**2.10 Surface area and pore size of SnO<sub>2</sub>-NiOx/Cu.**

**2.11 Raman spectra and calibration curves of VOCs at various concentrations.**

**2.12 Cross reactions for PYR, 2-NT and EBZA SERS sensing.**

**2.13 Schematic diagram of conversion from Raman mapping images to barcode.**

**2.14 Stability and reproducibility.**

**2.15 Comparison of the results obtained by the SERS nose with those obtained by GC-MS method.**

## **3 Supplementary Tables**

**3.1 Comparison of SnO<sub>2</sub>-NiOx/Cu with other CM-based SERS substrates.**

**3.2 Sensitivity of other sensors for VOC measurements.**

**3.3 The details in DFT calculation.**

## 1 Supplementary Methods

**1.1 Reagents and materials.** All chemicals were purchased from commercial suppliers and without further purification and modification. Nickel chloride hexahydrate ( $\text{NiCl}_2 \cdot 6\text{H}_2\text{O}$ ), tin(II) chloride dihydrate ( $\text{SnCl}_2 \cdot 2\text{H}_2\text{O}$ ), thiourea ( $\text{NH}_2\text{CSNH}_2$ , TU), cuprous chloride (CuCl), Copper(II) phthalocyanine (CuPc), Perfluorosulfonic acid (Nafion, 5 wt%), pyrene (PYR), 2-naphthalenethiol (2-NT) and 4-ethylbenzaldehyde (EBZA) were purchased from Sigma-Aldrich Inc. All of the other solvents were purchased from Aladdin Inc. All other chemicals were of analytical grade and the water used in the work was RNase-free.

**1.2 Instruments.** The structures and compositions of substrates were characterized by scanning electron micrographs (SEM), transmission electron micrographs (TEM), X-ray diffraction (XRD) and X-ray photoelectron spectra (XPS). The TEM images were obtained using a JEM2100 transmission electron microscope operated at an accelerating voltage of 200 kV. High resolution transmission electron micrographs (HRTEM) images were taking using a JEM-2100F transmission electron microscope with an accelerating voltage of 200kV. Spherical aberration-corrected transmission electron microscopes (ACTEM, Titan3 G2 60-300) were used to analyze higher-precision TEM images. SEM measurements were performed using a field emission gun S-4800 scanning electron microscope (Hitachi, Japan). XRD patterns were measured by a D/max2550VB3+/PC X-ray diffractometer using Cu (40 kV, 100 mA). XPS data were performed on a X-ray photoelectron spectroscopy (AXIS Ultra DLD, Japan) equipped with an Al  $K\alpha$  (1486.6eV photons). For SERS measurement and Raman mapping, Renishaw InVia Raman Microscope were used.

**1.3 Fabrication of  $\text{SnO}_2\text{-NiOx/Cu}$ ,  $\text{SnO}_2\text{-NiO}$  and  $\text{SnO}_2$ .** In a typical synthesis process, 0.1128 g of  $\text{SnCl}_2 \cdot 2\text{H}_2\text{O}$  was added into 45 mL of ethylene glycol to form a homogeneous solution. Subsequently, 0.22 g of thiourea was added with vigorous stirring at 30°C for 10 min. The mixture was then sealed in a Teflon lined stainless-steel autoclave and maintained at 245 °C for 24 h. After cooling naturally to room temperature, the solution emitted pungent odor and the resulting black product was collected by centrifugation and washed for 6 times with distilled water and absolute ethanol. The as-prepared precursor were annealed at 650 °C for 2 h in air to remove part of sulfur and oxidize Sn to  $\text{SnO}_2$ . The product was denoted as  $\text{SnO}_2$ . Then,  $\text{SnO}_2$  and 0.1782 g of  $\text{NiCl}_2 \cdot 6\text{H}_2\text{O}$  and 0.0496g CuCl were added into 45 mL of ethylene glycol to repeat above procedures to obtain  $\text{SnO}_2\text{-NiOx/Cu}$ .  $\text{SnO}_2\text{-NiO}$  was prepared without adding Cu source.

**1.4 Fabrication of  $\text{SnO}_2\text{-NiOx/Cu-CuPc}$  SERS nose.** The freshly prepared  $\text{SnO}_2\text{-NiOx/Cu}$  was dispersed in 5 mL  $10^{-10}$  M CuPc ethanol solution and magnetically stirred for 1 h. The products were collected by centrifugation (5,000 rpm, 5 min), washed three times with ethanol and self-assembled on silicon wafer.

**1.5 SERS measurements.** The substrates were placed inside a homemade chamber and incubated together with analytes of different concentrations at 60°C for 10 min. A 785 nm laser was used for all the measurements. In the vitro experiment, a 50× (NA 0.75) microscope objective with a working distance of 0.38 mm and spot focused laser was used. The laser power and acquisition time were 5 mW and 1 s, respectively.

**1.6 Photoelectrochemical measurements.** Photoelectrochemical (PEC) properties were measured using an Autolab potentiostat/galvanostat (Model PGSTAT 302N) in a three electrode cell with a Pt wire as the counter electrode and an Ag/AgCl reference electrode. NaOH (0.5 M) was used as electrolyte solution. The working electrode was prepared by dropping 10 mL of 1 mg mL<sup>-1</sup> SnO<sub>2</sub>-NiOx/Cu dispersion in 0.5 wt% of Nafion onto a precleaned FTO electrode and then let it dried in air at room temperature.

**1.7 Calculation of EF values on SnO<sub>2</sub>-NiOx/Cu, SnO<sub>2</sub>-NiO and SnO<sub>2</sub>.** The EF values of SnO<sub>2</sub>-NiOx/Cu, SnO<sub>2</sub>-NiO and SnO<sub>2</sub> were calculated according to the formula:

$$EF = (I_{SERS}/N_{SERS})(I_{bulk}/N_{bulk}) \quad (1)$$

$$N_{SERS} = CV N_A A_{Raman} / A_{Sub} \quad (2)$$

$$N_{bulk} = \rho h A_{Raman} N_A / M \quad (3)$$

where  $I_{SERS}$  and  $I_{bulk}$  are the intensities of the selected Raman peak in the SERS and normal Raman spectra, and  $N_{SERS}$  and  $N_{bulk}$  are the average number of molecules in the scattering area on the SERS and non-SERS substrates, respectively. The data of CuPc (10 μM, 10 μM and 0.01 nM) on the non-SERS Si/SiO<sub>2</sub> wafer were used as the normal Raman reference. Specifically, the intensity was averaged from the data on 20 random spots, and the number of analyte molecules within the scattering area was estimated by equation 2 on the assumption of a uniform distribution of the analyte molecules on the substrates.  $C$  is the molar concentration of the analyte solution,  $V$  is the volume of the droplet, and  $N_A$  is the Avogadro constant.  $A_{Raman}$  is the laser spot area (1 μm in diameter) of the Raman scanning. 20 μL of the analyte solution on substrate spread spontaneously into a square of about 3.6 mm in diameter after the solvent evaporated. The effective area of the substrate  $A_{Sub}$  can then be obtained. For bulk CuPc with a molecular weight ( $M$ ) of 576.1 g/mol and density ( $\rho$ ) of 1.62 g·cm<sup>-3</sup>, the confocal depth ( $h$ ) of the laser beam is 29 μm, and  $N_{bulk}$  can be calculated by Supplementary equation 3. The EF values of SnO<sub>2</sub>-NiOx/Cu, SnO<sub>2</sub>-NiO and SnO<sub>2</sub> were calculated to be as high as  $2.12 \times 10^5$ ,  $1.70 \times 10^5$  and  $1.66 \times 10^{10}$  (Fig. S4).

**1.8 Time-resolved diffuse reflectance (TDR) Spectroscopy.** TDR experiments were conducted using a regeneratively amplified Ti: sapphire laser system. Samples were irradiated with 785 nm laser light in 2 mm glass cuvettes with 110 fs, 0.2-0.5 μJ, pulses focused to a 100 μm diameter spot. The optical density at the excitation wavelength was maintained at 0.5-0.7. Transient spectra were acquired for 5 s per pump-probe time delay point. Spectra were constructed by merging the kinetic traces (binned to 3 ns steps, 100 laser shots per kinetic trace). All of the TDR data were corrected for group delay dispersion (GDD, or ‘chirp’) and  $t_0$  prior to kinetic analysis.

**1.9 DFT computational details.** First-principle density functional theory (DFT) with D3 dispersion correction<sup>S1</sup> was used for the optimization using the Vienna ab initio simulation package (VASP)<sup>S2-4</sup>. The Perdew-Burke-Ernzerhof form of Generalized Gradient Approximation (GGA-PBE) functional<sup>S5</sup> was used to obtain the exchange and correlation terms. The core electrons were substituted by the projector-augmented wave (PAW) pseudopotentials<sup>S6</sup>. The bulk structures of SnO<sub>2</sub> (space group: P42/mnm), SnO<sub>2</sub>-NiO (space group: R $\bar{3}$ ) and SnO<sub>2</sub>-NiO<sub>x</sub>/Cu (space group: P2/m) were taken from Materials project<sup>S7</sup>. Then the optimized bulk was obtained when the energy was converged to  $1 \times 10^{-7}$  eV and the forces were smaller than 0.015 eV/Å with a k-mesh of  $11 \times 11 \times 11$  and an energy cutoff of 550eV. The details of cell parameters and bulk structures are shown in Supplementary Table 1.

Three-layer surfaces were modeled in all cases as shown in Supplementary Table 3. It is determined experimentally that the miller index of SnO<sub>2</sub> surface was (110), while for the SnO<sub>2</sub>-NiO and SnO<sub>2</sub>-NiO<sub>x</sub>/Cu surfaces, indices including (110), (111) and (200) were also detected. The synthesizing environment of all the surfaces was the same, which implies the similarity of the surface termination of the three surfaces. In the determined SnO<sub>2</sub>(110) surface, it was confirmed that the most stable surface was terminated with O atoms with a surface energy of 0.091 eV/Å<sup>2</sup>. In the SnO<sub>2</sub>-NiO case, the O-terminated (110) surface has a surface energy of 0.130 eV/Å<sup>2</sup>, which is less stable than the one in (100) index (for simplification, here the (100) index was used to substitute (200) due to the same termination configuration they have) with a surface energy of 0.097 eV/Å<sup>2</sup>. Similarly, in the SnO<sub>2</sub>-NiO<sub>x</sub>/Cu case, the most stable surface with O-termination was also chosen for the following calculation as show in Supplementary Table 3.

To avoid the interaction between two layers, a 15 Å vacuum layer was added at the top of each surface. Only the top layer was relaxed during the optimization, and the bottom two layers were fixed as bulk layers. The surface optimization was done with an energy cutoff of 450eV with a k-mesh of  $3 \times 3 \times 1$ , and an energy and force convergence of  $1 \times 10^{-5}$  eV and 0.02 eV/Å respectively. Spin-polarized calculations were used in the Ni-included systems.

The molecules in gas phase were optimized with a large vacuum box of  $20 \times 20 \times 20$  Å<sup>3</sup>. The adsorption of molecules on the surfaces was computed under the same setting as mentioned before in the optimization of the bare surfaces. The adsorption energy of the molecules on the surfaces were calculated as:

$$E_{\text{ads}} = E_{\text{molecule@slab}} - E_{\text{slab}} - E_{\text{molecule}} \quad (1)$$

where  $E_{\text{molecule@slab}}$ ,  $E_{\text{slab}}$  and  $E_{\text{molecule}}$  are the electronic energy of the molecules adsorbed on the slab, the slab and the molecules in gas phase.

The optimized CuPC@slab structures and corresponding adsorption energies are shown in Supplementary Table 3.

Similarly, the charge density difference  $\Delta\rho$  is defined as follows:

$$\Delta\rho = \rho_{\text{molecule@slab}} - \rho_{\text{slab}} - \rho_{\text{molecule}} \quad (2)$$

where  $\rho_{\text{molecule@slab}}$ ,  $\rho_{\text{slab}}$  and  $\rho_{\text{molecule}}$  are the total charge density of the molecules adsorbed on the slab, the slab and the molecules in gas phase. The amount of charge transfer between molecules and surfaces was calculated by the bader charge analysis<sup>S8,9</sup>.

## 2 Supplementary Figures

### 2.1 Size distribution of SnO<sub>2</sub>-NiOx/Cu.

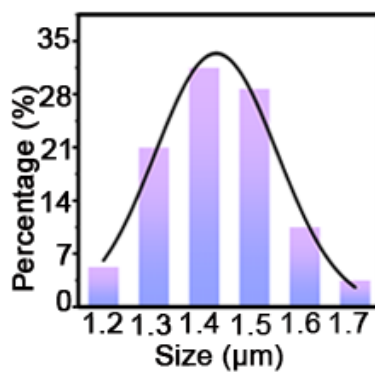


Figure S1. Size distribution of SnO<sub>2</sub>-NiOx/Cu.

### 2.2 Characterization of SnO<sub>2</sub> and SnO<sub>2</sub>-NiO.

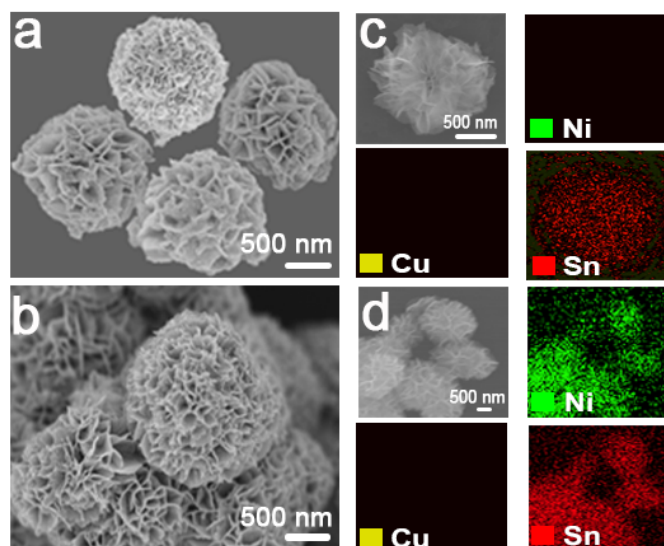
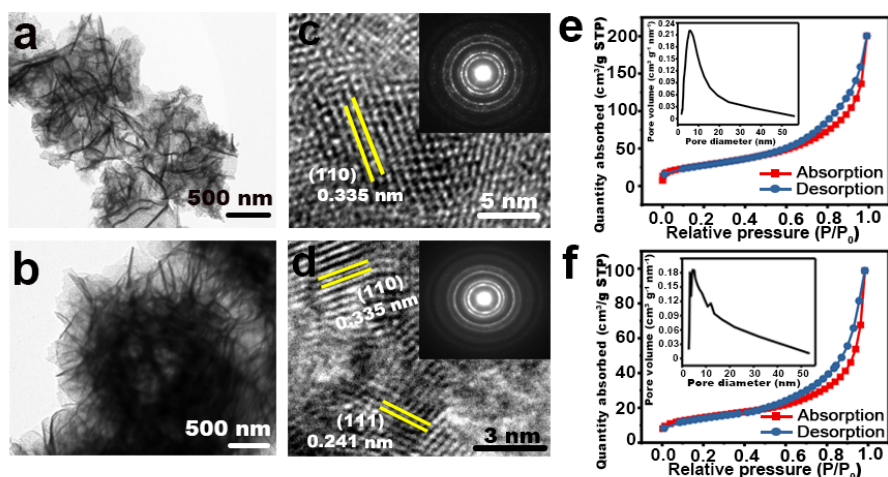
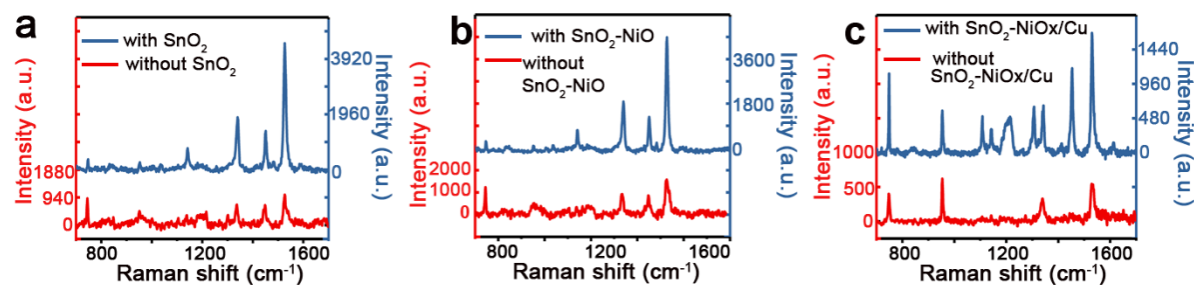


Figure S2. SEM images of (a) SnO<sub>2</sub> and (b) SnO<sub>2</sub>-NiO. EDS mapping images of (c) SnO<sub>2</sub> and (d) SnO<sub>2</sub>-NiO.



**Figure S3.** TEM images of (a) SnO<sub>2</sub> and (b) SnO<sub>2</sub>-NiO. HRTEM images of (c) SnO<sub>2</sub> and (d) SnO<sub>2</sub>-NiO. Insets: SAED patterns of the corresponding nanoparticles. Typical nitrogen adsorption-desorption isotherm and pore size distribution plots (inset) of (e) SnO<sub>2</sub> and (f) SnO<sub>2</sub>-NiO.

### **2.3 Raman spectra for calculation of EFs on SnO<sub>2</sub>, SnO<sub>2</sub>-NiO and SnO<sub>2</sub>-NiOx/Cu.**



**Figure S4.** Raman spectra of CuPc for EF value calculations on (a) SnO<sub>2</sub>, (b) SnO<sub>2</sub>-NiO and (c) SnO<sub>2</sub>-NiOx/Cu. (laser power: 5 mW, exposure time: 1 s, 50X lens).

### **2.4 Mott-Schottky plots and SAED patterns of SnO<sub>2</sub>-NiOx/Cu.**

It is well-known that NiOx/Cu is a p-type semiconductor and SnO<sub>2</sub> is a n-type semiconductor. Mott-Schottky plots presented in Fig. S5a provided the direct evidence for the existence of p-n junction. For SnO<sub>2</sub>-NiOx/Cu, the slope of Mott-Schottky plots above -0.15 V vs. Ag/AgCl was positive whereas that below -0.15 V was negative, indicating the existence of both n- and p-type characteristics. This result was consistent with the typical “V-shaped” Mott-Schottky plot of p-n junctions<sup>S10</sup>.

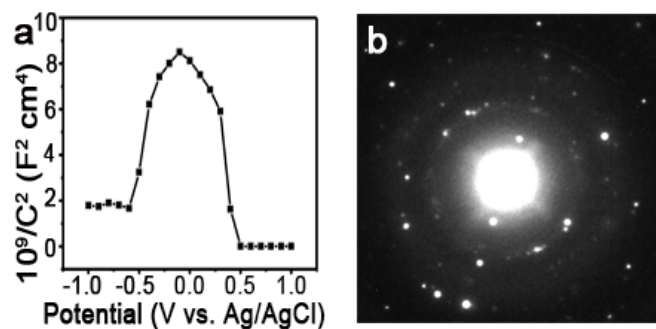


**Figure S5.** (a) Mott-Schottky plot of SnO<sub>2</sub>-NiO<sub>x</sub>/Cu in dark. (b) SAED patterns of SnO<sub>2</sub>-NiO<sub>x</sub>/Cu.

### 2.5 XPS survey spectrum of SnO<sub>2</sub>-NiO<sub>x</sub>/Cu.

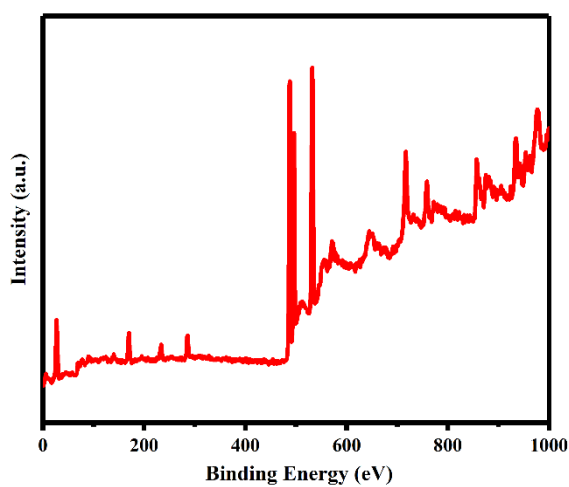


**Figure S6.** XPS survey spectrum of SnO<sub>2</sub>-NiO<sub>x</sub>/Cu.

### 2.6 TDR spectroscopic measurements.

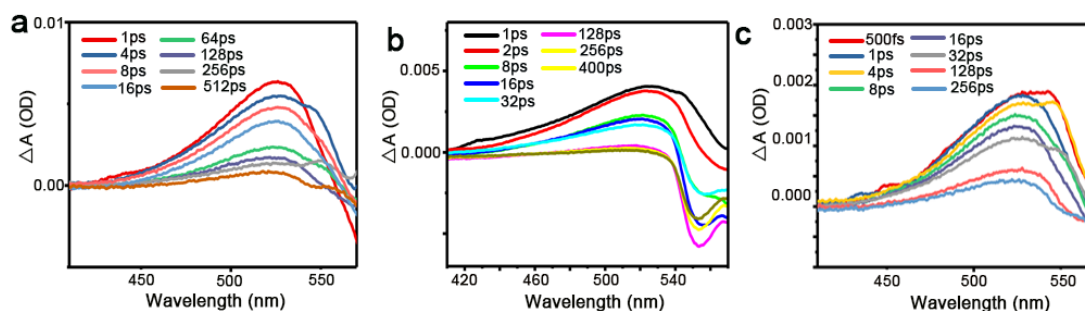


**Figure S7.** TDR spectroscopic measurements for (a) CuPc-SnO<sub>2</sub>, (b) CuPc-SnO<sub>2</sub>-NiO and (c) CuPc-SnO<sub>2</sub>-NiO<sub>x</sub>/Cu after irradiation with a 785-nm laser flash. OD, optical density.

## 2.7 Determination of band gaps.

The band gap energy of NiO, SnO<sub>2</sub>, SnO<sub>2</sub>-NiO, and SnO<sub>2</sub>-NiOx/Cu was determined from the plot of the plot of  $[F(R)h\nu]^2$  against  $h\nu$ , as revealed in Fig. S8b. The estimated band gaps for NiO, SnO<sub>2</sub>, SnO<sub>2</sub>-NiO, and SnO<sub>2</sub>-NiOx/Cu were therefore about 3.4, 2.8, 3.1 and 1.9 eV, respectively.

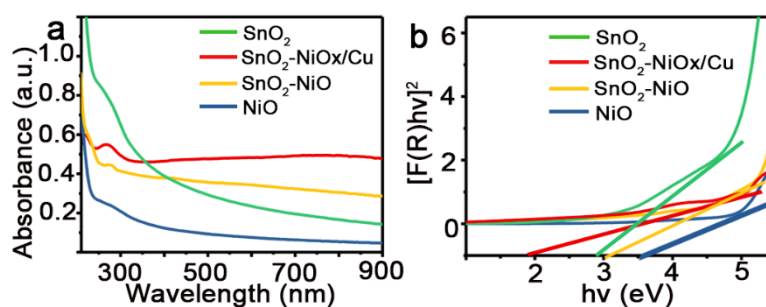


**Figure S8.** (a) UV-Vis absorption spectra of NiO, SnO<sub>2</sub>, SnO<sub>2</sub>-NiO, and SnO<sub>2</sub>-NiOx/Cu. (b) The plots of Kubelka-Munk relation for NiO, SnO<sub>2</sub>, SnO<sub>2</sub>-NiO, and SnO<sub>2</sub>-NiOx/Cu.

## 2.8 Effect of p-n heterojunction on Raman enhancement.

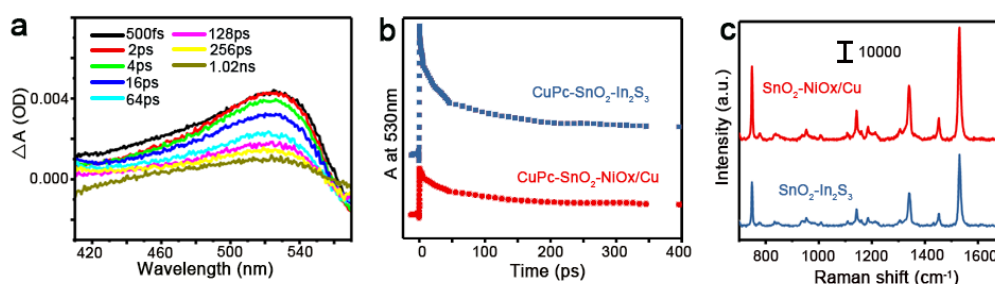


**Figure S9.** (a) TDR spectroscopic measurements for CuPc-SnO<sub>2</sub>-In<sub>2</sub>S<sub>3</sub> after irradiation with a 785-nm laser flash. OD, optical density. (b) Time profiles of normalized transient absorption at 530 nm of CuPc-SnO<sub>2</sub>-In<sub>2</sub>S<sub>3</sub> and CuPc-SnO<sub>2</sub>-NiOx/Cu. (c) Raman spectra of CuPc on SnO<sub>2</sub>-NiOx/Cu and SnO<sub>2</sub>-In<sub>2</sub>S<sub>3</sub> under a 785 nm laser (5 mW) with an exposure time of 0.5 s.

## 2.9 EM effect on SERS enhancement.

Since the band gap between HOMO of 4-Mercaptobenzoic acid (4-MBA) and CB of SnO<sub>2</sub> (2.24 eV) was larger than the energy of 785 nm laser (1.58 eV) (Figure S10), CT process between SnO<sub>2</sub>-NiOx/Cu substrate and 4-MBA was hard to be observed. Thus, 4-MBA was used as a signal molecule to evaluate the contribution of EM effect on SERS enhancement of SnO<sub>2</sub>-NiOx/Cu. The EF value was calculated to be  $7.48 \times 10^2$  for 4-MBA on SnO<sub>2</sub>-NiOx/Cu, which was 8 orders of magnitude lower than that of CuPc on SnO<sub>2</sub>-NiOx/Cu. Consequently, the EM effect on SERS enhancement of SnO<sub>2</sub>-NiOx/Cu was very limited.

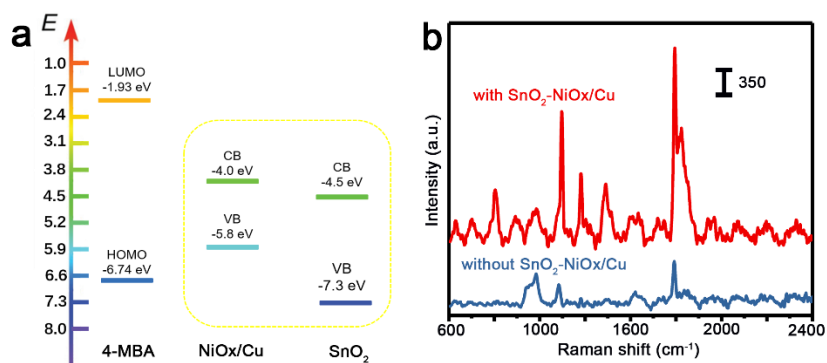


**Figure S10.** (a) Energy levels of 4-MBA and SnO<sub>2</sub>-NiOx/Cu. (b) Raman spectra of 4-MBA (1 mM) for EF value calculation on SnO<sub>2</sub>-NiOx/Cu (laser power: 5 mW, exposure time: 1 s, 50X lens).

### 2.10 Surface area and pore size of SnO<sub>2</sub>-NiOx/Cu.

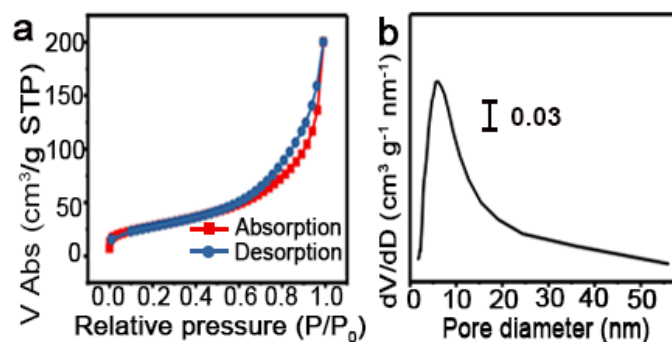


**Figure S11.** (a) Typical nitrogen adsorption-desorption isotherm and (b) pore size distribution plot of SnO<sub>2</sub>-NiOx/Cu.

### 2.11 Raman spectra and calibration curves of VOCs at various concentrations.

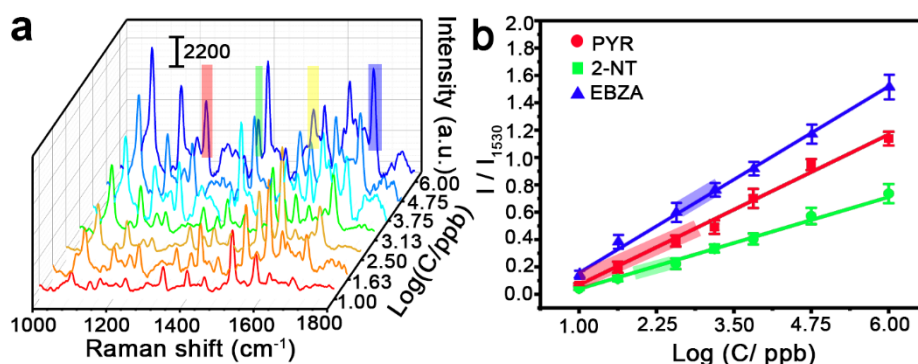


**Figure S12.** (a) Raman spectra of SnO<sub>2</sub>-NiOx/Cu-CuPc obtained with PYR, 2-NT and EBZA at various concentrations: 10, 10<sup>1.63</sup>, 10<sup>2.50</sup>, 10<sup>3.13</sup>, 10<sup>3.75</sup>, 10<sup>4.75</sup> and 10<sup>6.00</sup> ppb. (b) Calibration curves of PYR, 2-NT and EBZA on a semilog scale.

## 2.12 Cross reactions for PYR, 2-NT and EBZA SERS sensing.

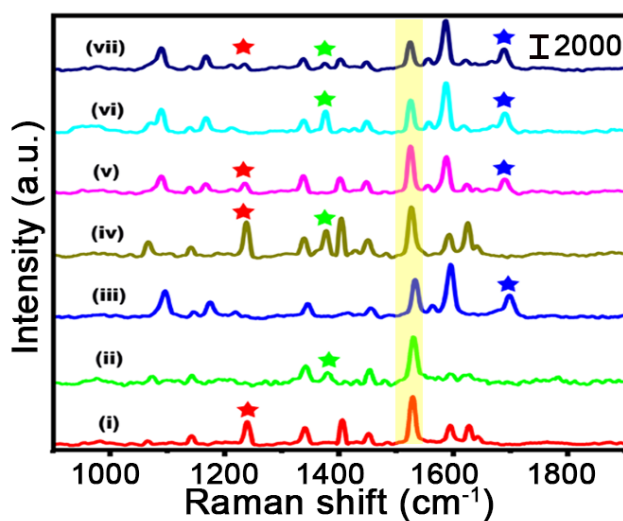


**Figure S13.** SERS spectra for (i) Pyrene, (ii) 2-NT, (iii) EBZA, (iv) Pyrene and 2-NT, (v) Pyrene and EBZA, (vi) 2-NT and EBZA and (vii) Pyrene, 2-NT and EBZA with a concentration of 1 ppm.

## 2.13 Schematic diagram of conversion from Raman mapping images to barcode.

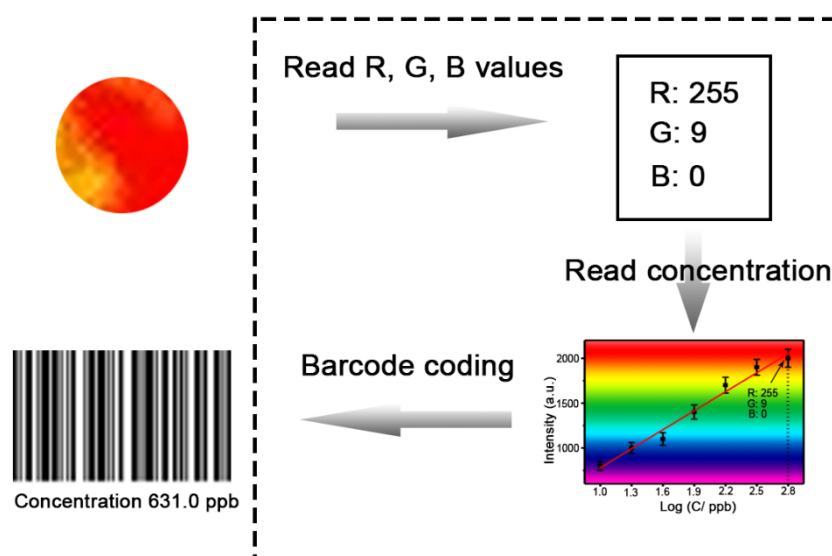


**Figure S14.** Schematic diagram of conversion from Raman mapping images to barcode. First, read R, G, B values of the Raman mapping images. Secondly, according to the standard curve chromaticity diagram, the RGB values were converted into the corresponding concentrations. Thirdly, the concentrations were directly encoded into a barcode for electronic reading. The entire process was automatically obtained by a computer.

## 2.14 Stability and reproducibility.

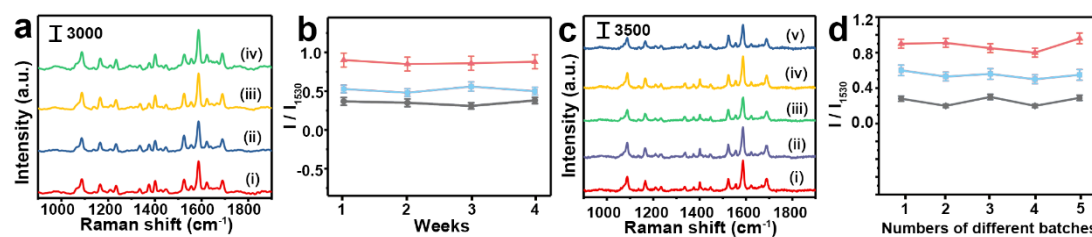


**Figure S15.** (a) SERS spectra and (b) SERS intensities for VOCs (10<sup>-5</sup> M of pyrene, 2-NT and EBZA) on SnO<sub>2</sub>-NiO<sub>x</sub>/Cu-CuPc nose after incubation with the SERS nose for (i) one, (ii) two, (iii) three and (iv) four weeks. (c) SERS spectra and (d) SERS intensities for 5 individual tests of 10<sup>-5</sup> M of pyrene, 2-NT and EBZA using the presented SERS nose.

## 2.15 Comparison of the results obtained by the SERS nose with those obtained by GC-MS method.

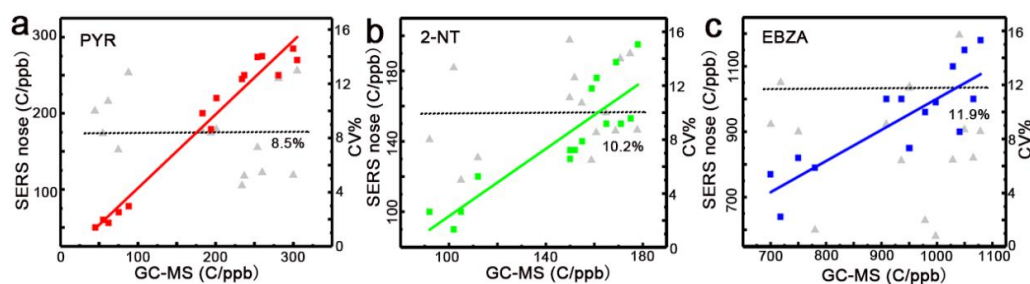


**Figure S16.** Passing-Boblok regression analyses between the results obtained by the present SERS nose and those obtained by GC-MS method of (a) PYR, (b) 2-NT and (c) EBZA from 10<sup>1.6</sup> to 10<sup>2.3</sup> ppb, 10<sup>1.9</sup> to 10<sup>2.3</sup> ppb and 10<sup>2.8</sup> to 10<sup>3.2</sup> ppb, respectively.

### 3 Supplementary Tables

#### 3.1 Comparison of SnO<sub>2</sub>-NiOx/Cu with other CM-based SERS substrates.

**Table S1. Comparison of SnO<sub>2</sub>-NiOx/Cu with other CM-based SERS substrates.**

Raman substrate	Detection limit/ $\mu\text{M}$	EF value	Reference
MoS <sub>2</sub>	0.1	$3.4 \times 10^5$	S11
Ti <sub>3</sub> C <sub>2</sub> T <sub>x</sub> MXene	0.1	$1.2 \times 10^6$	S12
TiO <sub>2</sub> nanosheets	100	$1.86 \times 10^6$	S13
ZnO Nanocages	100	$6.62 \times 10^5$	S14
MoO <sub>2</sub>	0.01	$4.8 \times 10^6$	S15
PDA-coated MoO <sub>3-x</sub> nanosheets	$10^{-10}$	$1 \times 10^{10}$	S16
W <sub>18</sub> O <sub>49</sub> /monolayer	$10^{-9}$	$3.45 \times 10^7$	S17
MoS <sub>2</sub> SnO <sub>2</sub> -NiOx/Cu	$10^{-11}$	$1.66 \times 10^{10}$	This work

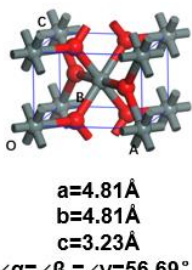
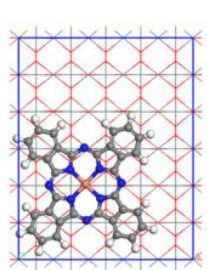
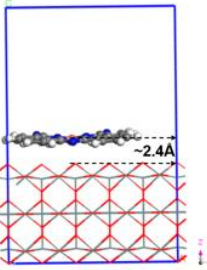
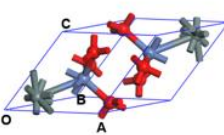
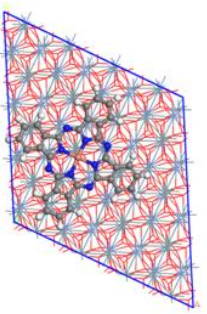
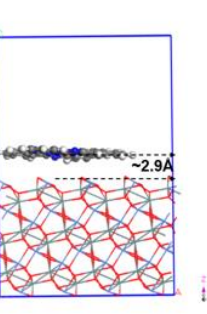
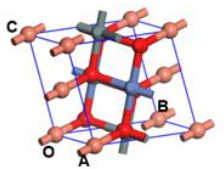
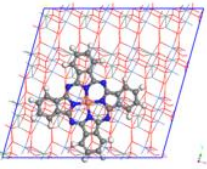
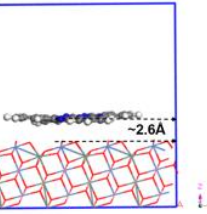
#### 3.2 Sensitivity of other sensors for VOC measurements.

**Table S2. Sensitivity of other sensors for VOC measurement.**

Method	Analyte	LOD/ppb	Reference
GC-MS	Pyrene	50	S18
	EBZA	18.6	S19
Fluorescence	Pyrene	60.68	S20
	2-NT	$1.17 \times 10^3$	S21
	EBZA	$6 \times 10^4$	S22
Electrochemistry	Pyrene	350	S23
	2-NT	$1.6 \times 10^3$	S24

### 3.3 The details in DFT calculation.

**Table S3.** Optimized bulk and CuPc@(SnO<sub>2</sub>, SnO<sub>2</sub>-NiO, SnO<sub>2</sub>-NiO<sub>x</sub>/Cu) surface structures. Atomic color codes are: O (red), Sn (grey), Ni (blue grey), Cu (coral), H (white), N (blue) and C (brown).

Type	Bulk	Top	Side	E <sub>ads</sub> /eV
CuPC@SnO <sub>2</sub> (110) 3 layers p(5x3)	 <p> <math>a=4.81\text{\AA}</math>  <math>b=4.81\text{\AA}</math>  <math>c=3.23\text{\AA}</math>  <math>\angle\alpha=\angle\beta=\angle\gamma=56.69^\circ</math> </p>		 <p>~2.4Å</p>	-3.95
CuPC@SnO <sub>2</sub> -NiO(100) 3 layers p(4x4)	 <p> <math>a=b=c=5.58\text{\AA}</math>  <math>\angle\alpha=\angle\beta=\angle\gamma=56.69^\circ</math> </p>		 <p>~2.9Å</p>	-2.99
CuPC@SnO <sub>2</sub> -NiO <sub>x</sub> /Cu(110) 3 layers p(3x4)	 <p> <math>a=3.18\text{\AA}</math>  <math>b=6.12\text{\AA}</math>  <math>c=5.37\text{\AA}</math>  <math>\angle\alpha=107.8^\circ</math>  <math>\angle\beta=\angle\gamma=90.0^\circ</math> </p>		 <p>~2.6Å</p>	-4.01

## Reference

- S1 Grimme, S., Antony, J., Ehrlich, S. & Krieg, H. A consistent and accurate ab initio parametrization of density functional dispersion correction (DFT-D) for the 94 elements H-Pu. *J. Chem. Phys.* **132**, 154104 (2010).
- S2 Kresse, G. & Furthmüller, J. Efficient iterative schemes for ab initio total-energy calculations using a plane-wave basis set. *Phys. Rev. B - Condens. Matter Mater. Phys.* **54**, 11169-11186 (1996).
- S3 Kresse, G. & Furthmüller, J. Efficiency of abinitio total energy calculations for metals and semiconductors using a plane-wave basis set. *Comput. Mater. Sci.* **6**, 15-50 (1996).
- S4 Kresse, G. & Hafner, J. Ab initio molecular dynamics for liquid metals. *Phys. Rev. B* **47**, 558-561 (1993).
- S5 Perdew, J. P., Burke, K. & Ernzerhof, M. Generalized gradient approximation made simple. *Phys. Rev. Lett.* **78**, 1396-1396 (1996).
- S6 Kresse, G. & Joubert, D. From ultrasoft pseudopotentials to the projector augmented-wave method. *Phys. Rev. B - Condens. Matter Mater. Phys.* **59**, 1758-1775 (1999).
- S7 <https://materialsproject.org/>.
- S8 Henkelman, G., Arnaldsson, A. & Jónsson, H. A fast and robust algorithm for Bader decomposition of charge density. *Comput. Mater. Sci.* **36**, 354-360 (2006).
- S9 Bader, R. F. W. *Atoms in Molecules — a Quantum Theory*. *Journal of Molecular Structure: THEOCHEM* (Oxford University Press, 1990). doi:10.1016/s0166-1280(96)90925-2.
- S10 Meng, F., Li, J., Cushing, S. K., Zhi, M. & Wu, N. Solar hydrogen generation by nanoscale p-n junction of p-type molybdenum disulfide/n-type nitrogen-doped reduced graphene oxide. *J. Am. Chem. Soc.* **135**, 10286-10289 (2013).
- S11 Zheng, Z. et al. Semiconductor SERS enhancement enabled by oxygen incorporation. *Nat. Comm.*, **8**, 1993 (2017).
- S12 Sarycheva, A. et al. Two-dimensional titanium carbide (MXene) as surface-enhanced Raman scattering substrate. *J. Phys. Chem. C* **121**, 19983-19988 (2017).
- S13 Wang, X. et al. Two-dimensional amorphous TiO<sub>2</sub> nanosheets enabling high efficiency photoinduced charge transfer for excellent SERS activity. *J. Am. Chem. Soc.* **141**, 5856-5862 (2019).
- S14 Wang, X. et al. Remarkable SERS activity observed from amorphous ZnO nanocages. *Angew. Chem. Int. Ed.* **56**, 9851-9855 (2017).
- S15 Zhang, Q. et al. Plasmonic MoO<sub>2</sub> nanospheres as a highly sensitive and stable non-noble metal substrate for multicomponent surface-enhanced Raman analysis. *Anal. Chem.* **89**, 11765-11771 (2017).
- S16 Wang, J. et al. Stable and tunable plasmon resonance of molybdenum oxide nanosheets from the ultraviolet to the near-infrared region for ultrasensitive surface-enhanced Raman analysis. *Chem. Sci.* **10**, 6330-6335 (2019)
- S17 Li, M., Fan, X., Gao, Y. & Qiu, T. W<sub>18</sub>O<sub>49</sub>/monolayer MoS<sub>2</sub> heterojunction-enhanced Raman scattering. *J. Phys. Chem. Lett.* **10**, 4038-4044 (2019).
- S18 McDonald, T. J., Wang, B., McDonald, S. J. & Brooks, J. M. Quantitative determination of

- aromatic hydrocarbons using selected ion monitoring gas chromatography/mass spectrometry TDI-Brooks International; College Station, TX, 2006.
- S19 Ji, S., Gu, S., Wang, X. & Wu, N. Comparison of olfactometrically detected compounds and aroma properties of four different edible parts of Chinese mitten crab. *Fish Sci.* **81**,1157-1167 (2015).
- S20 Mohr, A. et al. A new pyrene-based fluorescent probe for the determination of critical micelle concentrations. *J. Phys. Chem. B* **111**, 12985-12992 (2007).
- S21 Martínez, E., Rodríguez, J. A., Bautista, M., Rangel-Vargas, E. & Santos, E. M. Use of 2-naphthalenethiol for derivatization and determination of acrylamide in potato crisps by high-performance liquid chromatographic with fluorescence detection. *Food Anal. Method* **11**,1636-1644 (2018).
- S22 Simoneau, C., Van den Eede, L. & Valzacchi, S. Identification and quantification of migration of chemicals from plastics baby bottles used as substitutes for polycarbonate. *Food Addit Contam* **29**, 469-480 (2012).
- S23 Penezić, A., Gašparović, B., Stipaničev, D. & Nelson, A. In situ electrochemical method for detecting freely dissolved polycyclic aromatic hydrocarbons in water. *Environ. Chem.* **11**, 173-180 (2014).
- S24 Duy, P. K., Yen, P. T. h., Chun, S., Ha, V. T. T. & Chung, H. Carbon fiber cloth-supported Au nanodendrites as a rugged surface-enhanced Raman scattering substrate and electrochemical sensing platform. *Sens. Actuators B Chem.* **225**, 377-383 (2016).